PCCP

First-Principles Study of Strain Effect on Thermoelectric Properties of LaP and LaAs

Journal:	*Physical Chemistry Chemical Physics*
Manuscript ID	CP-ART-06-2021-002871.R1
Article Type:	Paper
Date Submitted by the Author:	21-Jul-2021
Complete List of Authors:	Lin, Chia-Min; The University of Alabama at Birmingham, Department of Physics Chen, Wei-Chih; The University of Alabama at Birmingham, Department of Physics Chen, Cheng-Chien; The University of Alabama at Birmingham, Department of Physics

PCCP

ARTICLE TYPE

Cite this: DOI: 00.0000/xxxxxxxxxx

First-Principles Study of Strain Effect on Thermoelectric Properties of LaP and LaAs†

Chia-Min Lin, Wei-Chih Chen, and Cheng-Chien Chen*

Received Date
Accepted Date

DOI: 00.0000/xxxxxxxxxx

Rare-earth monopnictides have attracted much attention due to their unusual electronic and topological properties for potential device applications. Here, we study rock-salt structured lanthanum monopnictides LaX (X = P, As) by density functional theory (DFT) simulations. We show systematically that a meta-GGA functional combined with scissor correction can efficiently and accurately compute electronic structures on a fine DFT k-grid, which is necessary for converging thermoelectric calculations. We also show that strain engineering can effectively improve thermoelectric performance. Under the optimal condition of 2% isotropic tensile strain and carrier concentration $n = 3 \times 10^{20}$ cm^{-3}, LaP at temperature 1200 K can achieve a figure of merit ZT value > 2, which is enhanced by 90% compared to the unstrained value. With carrier doping and strain engineering, lanthanum monopnictides thereby could be promising high-temperature thermoelectric materials.

1 INTRODUCATION

Thermoelectric materials can directly convert heat into electricity, and they have various existing and potential applications in energy sector and powering industry[1–6]. Thermoelectric technology is eco-friendly, where the thermal source can be waste heat, fuels, as well as geothermal and solar energy. Small-scale thermoelectric devices can be made as power supply for electricity generation or as refrigerator for cooling purpose. In all these applications, achieving a high thermoelectric efficiency is crucial. The performance of thermoelectric materials can be determined by the dimensionless figure of merit ZT:

$$ZT = \frac{S^2\sigma T}{\kappa} = \frac{S^2\sigma T}{(\kappa_e + \kappa_L)}. \quad (1)$$

Here, the Seebeck coefficient S is a measure of induced voltage due to temperature difference across a material. σ is the electrical conductivity, T is the temperature, and κ is total thermal conductivity, which has both electronic (κ_e) and lattice (κ_L) contributions. $ZT \geq 1$ is considered suitable for practical thermoelectric applications, and there is an ongoing need to develop larger ZT materials that are functional at different temperatures[7–9].

Several approaches have been proposed to improve thermoelectric performance, ranging from band- and nano-structure engineering[10–14], application of strain[15,16], to the search of new quantum materials[17,18]. Based on the definition in Eq. (1), a high ZT value requires large S, large σ, and/or small κ. In many cases, however, these requirements cannot be satisfied simultaneously due to the trade-off relationships between different parameters. For example, a larger carrier concentration can enhance σ, but it can reduce S as well. Also, materials with high σ often exhibits large κ_e. Moreover, while ZT has an explicit linear T dependence, S can degrade at high temperature due to bipolar excitation of both hole and electron carriers[19–22]. Therefore, increasing ZT remains a nontrivial and challenging task.

In this paper, we study the effects of doping and strain on lanthanum monopnictides LaX (X = P, As), which are promising high-temperature thermoelectric materials. LaX with the rock-salt structure belong to a large group of rare-earth pnictides[23], and they have been widely investigated due to their thermal stability, mechanical strength, as well as exotic electronic and topological properties[24–32]. However, the rare-earth element and its correlated orbitals near the Fermi level have posed challenges for first-principles band-theory studies. In particular, it has been a debate whether the systems are metallic or semiconducting[33–36]. Deligoz *et al.* found that LaP and LaAs are metals, based on density functional theory (DFT) with the local-density approximation (LDA)[37]. However, Charifi *et al.* found that LaN, LaP, and LaAs are semiconductors using both LDA and the generalized gradient approximation (GGA) calculations[38]; Shoaib *et al.*[39] also reached a similar conclusion using the Wu and Cohen GGA functional[40]. Moreover, Yan *et al.*[41] and Khalid *et al.*[42] reported nonzero energy gaps in LaP and LaAs, by using a more sophisticated Heyde-Scuseriae-Ernserh hybrid functional (HSE06). Since the band structure and energy gap play crucial roles in determining transport and thermoelectric properties, it is important to ensure

Department of Physics, University of Alabama at Birmingham, Birmingham, Alabama 35294, USA.

* E-mail: chencc@uab.edu

† Electronic Supplementary Information (ESI) available: Convergence tests of structural, electronic, phonon, and thermoelectric calculations.. See DOI: 10.1039/cXCP00000x/

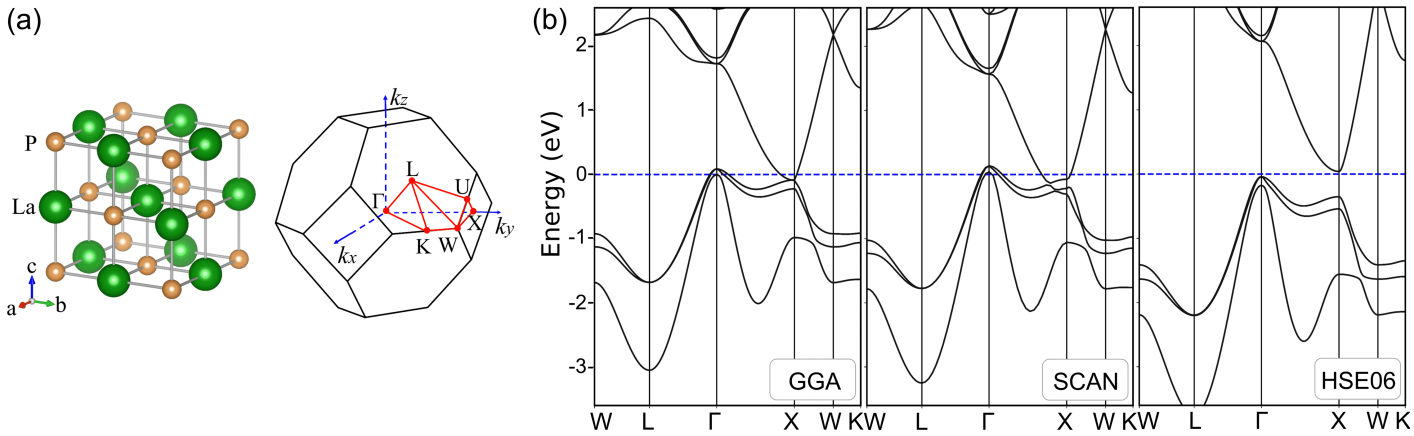

Fig. 1 (a) LaP face-centered cubic structure and its Brillouin zone. (b) Band structures along high-symmetry paths of the Brillouin zone computed respectively by GGA, SCAN, and HSE06 functionals for unstrained LaP. The zero energy corresponds to the Fermi level.

accurate description and computation of the electronic structures.

In the following, we perform systematic calculations by considering three different rungs of the "Jacob's ladder"[43], including GGA, meta-GGA, and hybrid DFT functionals. We show that meta-GGA calculations combined with a scissor correction method can provide accurate and converged thermoelectric results on a refined k-grid, which otherwise is not possible with a computationally much more expensive hybrid functional. We also show that isotropic strain and carrier doping are effective means to manipulate the transport properties of LaX for potential high-temperature thermoelectric applications.

2 COMPUTATIONAL METHODS

The properties of LaX (X = P, As) are investigated by density functional theory (DFT)[44,45] using a plane wave pseudopotential method as implement in the Vienna *ab initio* simulation package (VASP)[46,47]. We use a plane wave energy cutoff of 500 eV, which is 30% larger than the recommended value in VASP pseudopotential files, and it suffices to converge the DFT total energy with a difference $< 10^{-4}$ eV/atom. For each material, we first relax the lattice parameters to obtain the unstrained rock-salt structures using the Perdew-Burke-Ernzerhof generalized gradient approximation (GGA-PBE) functional[48]. After structure relaxation, we perform self-consistent electronic calculations with spin-orbit coupling respectively for three functionals: the GGA-PBE functional, the meta-GGA strongly-constrained and appropriately-normed (SCAN) functional[49], and the hybrid Heyde-Scuseriae-Ernserh (HSE06) functional[50,51]. Studying different advanced functionals beyond GGA will help determine the electronic band gap more accurately. The convergence criteria of self-consistent and structure calculations are set to 10^{-5} eV/unit cell and 10^{-4} eV/Å, respectively. The Monkhorst-Pack sampling scheme[52] is used with a Γ-centered k-point mesh of grid size $11\times11\times11$ (resolution = $0.01\times2\pi$/Å) points over the Brillouin zone.

For transport quantities – the Seebeck coefficient S, electrical conductivity σ, and electronic thermal conductivity κ_e – a much refined k-grid is needed to converge the calculations (see the Electronic Supplementary Information (ESI)† for convergence tests). Therefore, we compute transport properties using the meta-GGA SCAN functional with spin-orbit coupling on a denser k-gird of $41\times41\times41$ (resolution = $0.006\times2\pi$/Å) points. HSE06 calculations on such a k-grid is computationally too expensive to perform. On top of the meta-GGA calculations, we further introduce a scissor operator to correct the band gap, which plays a crucial role in determining the thermoelectric performance. With inputs from VASP calculations, transport quantities are computed by the BoltzTraP2 package[53]. Based on a linearized version of the Boltzmann transport equation, BoltzTraP2 evaluates the transport distribution function[54] under the rigid-band and constant relaxation time approximations. The transport coefficients S, σ, and κ_e can be computed directly once the transport distribution function is determined.

For phonon spectra and lattice thermal conductivity κ_L, we utilize respectively the Phonopy package[55] and the Phono3py code[56,57]. Phonopy computes the phonon dispersion based on the harmonic approximation, and it enables us to assure that the rock-salt structures of LaX (X = P, As) under study are dynamically stable (i.e. with only positive phonon modes). Phono3py solves linearized phonon Boltzmann transport equation with single-mode relaxation time approximation. Finite atomic displacements and supercell approaches with respectively $5\times5\times5$ and $4\times4\times4$ supercells are adopted to compute the second- and third-order force constants, which are required for evaluating phonon lifetimes and κ_L. A phonon q-point sampling mesh of $21\times21\times21$ points and a real-space cutoff approach up to the fourth neighbor (N-cutoff = 4, with a cutoff radius ~ 6.1 Å) are utilized to reduce the computational demand for the third-order force constants. The corresponding VASP calculations are based on the GGA-PBE functional without the spin-orbit coupling. Further Phonopy and Phono3py results and convergence tests are given in the ESI†. Finally, the theoretical crystal structure in our study is visualized by the VESTA software[58].

3 RESULTS AND DISCUSSION

We begin by discussing LaP, which has a stable face-centered cubic structure with space group symmetry $Fm\bar{3}m$ (No. 225). This rock-salt structure and its first Brillouin zone are shown in Fig. 1(a). In our structure relaxation calculation using a primi-

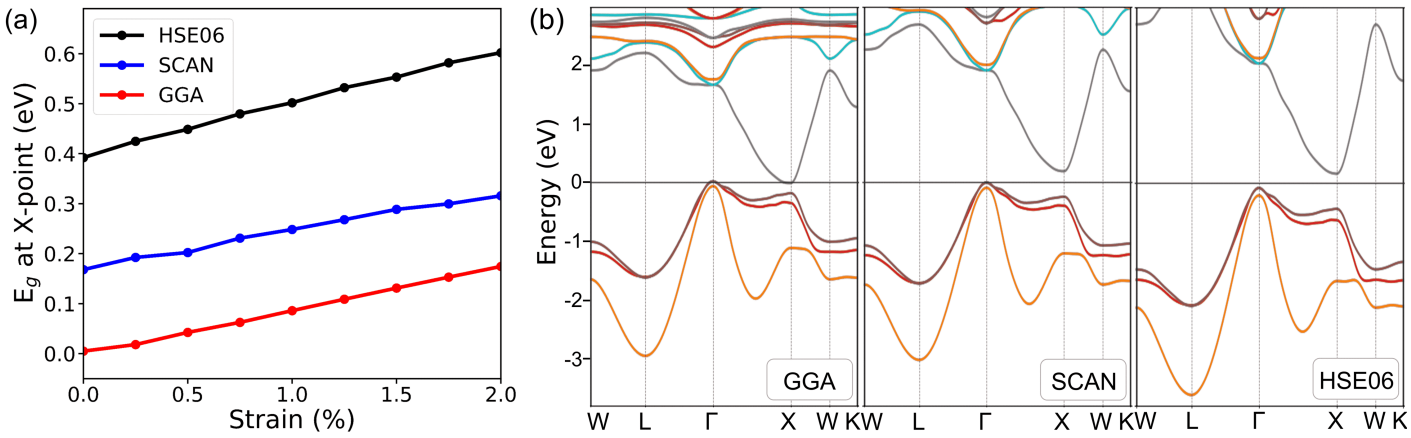

Fig. 2 (a) Band gaps at the X point for LaP computed as a function of isotropic strain using different functionals. (b) Band structures computed respectively by GGA, SCAN, and HSE06 functionals for LaP under 2% isotropic tensile strain. The zero energy corresponds to the Fermi level.

tive cell, the equilibrium lattice parameter of LaP is found to be $a = 4.278$ Å. The corresponding value in a conventional cell is $a = 6.050$ Å, which agrees with previous reports of $a = 6.034$ Å[41] and $a = 6.025$ Å[27]. With the unstrained structure, we compute the electronic band structures including spin-orbit coupling respectively for three different functionals: GGA, meta-GGA SCAN, and HSE06. As shown in Fig. 1(b), the GGA (left panel) and meta-GGA SCAN (middle panel) results indicate that LaP is a semimetal with band crossing (between predominantly La d- and P p-orbitals) near the X point. However, the HSE06 result (right panel) shows a band gap ~ 0.39 eV at the X point, indicating that LaP is a semiconductor, which agrees with previous studies using advanced DFT functionals[32,39,41]. It is known that GGA typically underestimates the energy gap. While the meta-GGA SCAN functional can improve the gap estimation[59], this improvement often remains insufficient. Basically, the simple functional forms of GGA and meta-GGA are not flexible enough to accurately reproduce both exchange correlation energy and its charge derivative[43]. On the other hand, the advanced hybrid functional HSE06 provides a more sophisticated nonlocal expression for more precise gap prediction.

Figure 2(a) shows how the X point band gap evolves with isotropic strain for different functionals. The gap values are obtained by band structure interpolations using BoltzTraP2 with inputs from VASP self-consistent calculations. Overall, the energy gap would increase under tensile strain, and its rate of increase with strain is similar for all three functionals. Figure 2(b) shows the interpolated band structures at the maximum value of $+2\%$ (tensile) strain under study, where the X point band gaps are 0.18 eV, 0.32 eV, and 0.60 eV, respectively for GGA, SCAN, and HSE06. We note again that converging the DFT total energy is much easier than converging thermoelectric calculations. As shown in the systematic studies in the ESI†, a very refined k-grid is needed to satisfactorily converge transport properties. For the results presented below, we adopt a dense k-grid of $41 \times 41 \times 41$ points, so the calculations can be performed only with the GGA and meta-GGA SCAN functionals. In addition, we further employ a scissor method and correct the GGA and meta-GGA band gaps to that of HSE06 based on Fig. 2(a), which provides a roadmap for band gap correction as a function of isotropic strain.

Figures 3(a) and 3(b) show the Seebeck coefficients S of unstrained LaP as a function of chemical potential μ at various temperatures, using respectively the GGA and meta-GGA SCAN functionals. The red vertical dashed line in Fig. 3 indicates the Fermi level E_f. As expected, S is positive when hole carriers dominate ($\mu - E_f < 0$), and S is negative when electron carriers dominate ($\mu - E_f > 0$). Compared to the GGA result [Fig. 3(a)], the peak strength of S in meta-GGA [Fig. 3(b)] is slightly enhanced due to an enlarged band gap. Figures 3(c) and 3(d) show similar calculations respectively for GGA and SCAN functionals with scissor correction. In both cases, the conduction bands overall are shifted up in energy by matching the X point gap to that of HSE06. The results of GGA with scissor correction [Fig. 3(c)] resemble closely those of SCAN with scissor correction [Fig. 3(d)], both showing that S is further enhanced after the gap correction. Therefore, the above results show that obtaining a proper band gap can play a dominant role in determining thermoelectric behaviors.

Figure 4(a) shows BoltzTraP2 calculations of the Seebeck coefficient S as a function of carrier density n at various temperature T, using the SCAN functional with scissor correction for unstrained LaP. Overall, S is enhanced with increasing T or decreasing n. These behaviors can be understood qualitatively using a nearly free electron picture with parabolic band and energy-independent scattering approximations[60,61]:

$$S = \frac{8\pi^2 k_B^2}{3eh^2} m^* T \left(\frac{\pi}{3n}\right)^{2/3}. \quad (2)$$

Here, e, k_B, h, and m^* are respectively electron charge, Boltzmann constant, Plank constant, and carrier effective mass. Equation (2) predicts that S depends linearly on T and varies as $n^{-2/3}$, which is consistent with Fig. 4(a) in the high carrier concentration regime. On the other hand, S also can decrease with increasing temperature in the low carrier concentration region, as shown in Fig. 4(a). This unusual situation is caused by a bipolar conduction (or finite-temperature excitation of both hole and electron carriers)[19–22]. The bipolar effect is more prominent in narrow-gap semiconductors (< 0.5 eV), and it can lead to degrading thermoelectric performance.

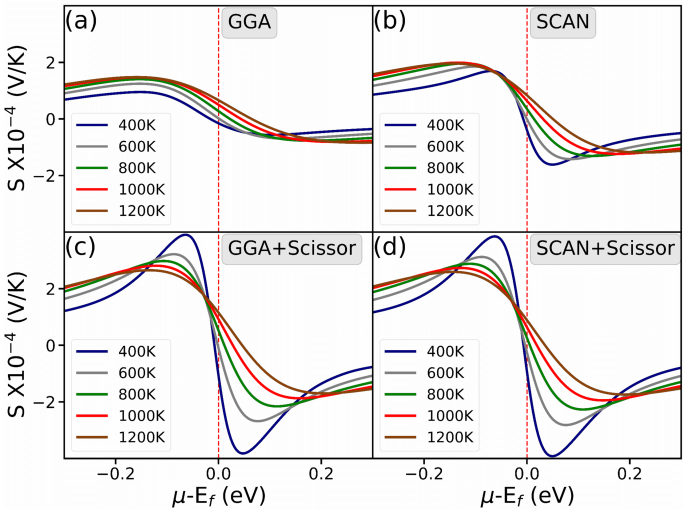

Fig. 3 Seebeck coefficients as a function of the chemical potential μ at different temperatures, computed for unstrained LaP using respectively (a) GGA functional,(b) SCAN functional, (c) GGA functional with scissor correction, and (d) SCAN functional with scissor correction.

Figure 4(b) shows the electrical conductivity σ divided by the relaxation time τ. Since it is more difficult to compute τ from first principles due to the complexity of different scattering mechanisms, here we simply adopt a typical value of $\tau = 1 \times 10^{-14}$ s. In general, σ shows a weak temperature dependence and decreases slightly with increasing T. Also as expected, σ increases with increasing n ($\sigma \propto n$), which is opposite to the behavior of Seebeck coefficient ($S \propto n^{-2/3}$). In addition, σ is expected to be inversely proportional to the effective mass m^*, while S depends linearly on m^*. For the above reasons, it is thereby challenging to enhance a material's thermoelectric power factor ($\equiv S^2\sigma$).

Figure 4(c) shows the electronic thermal conductivity κ_e divided by τ. In general, κ_e has a similar dependence on n as σ. However, κ_e has a stronger temperature dependence and increases with increasing T. These behaviors obey qualitatively the Wiedemann-Franz law[62]:

$$\kappa_e = \frac{\pi^2}{3}(\frac{k_B}{e})^2 \sigma T \equiv L\sigma T, \quad (3)$$

which is based on the fact that both heat and electrical transport involve free charge carriers in metals. Here, $L = 2.44 \times 10^{-8}\ W\Omega K^{-2}$ is the free-electron Lorentz number. Since $ZT \equiv S^2\sigma T/(\kappa_e + \kappa_L)$, for materials with high κ_e and low κ_L, or when $\kappa_e \gg \kappa_L$ at very high temperature, Eq. (3) dictates that $ZT \simeq S^2/L$ (independent of the choice of τ). In this case, a less dispersive flat band (which results in larger effective m^* and S) is expected to show a higher ZT value.

The actual ZT value of unstrained LaP is shown in Fig. 4(d), which is obtained from S, σ, and κ_e in Figs. 4(a)-4(c), as well as from the lattice thermal conductivity κ_L (to be discussed shortly in Fig. 5). The ZT value is highly dependent on the carrier concentration n and temperature T. For example, ZT has a peak value of 0.77 at $T = 800$ K near $n = 3 \times 10^{20}$ cm^{-3}. The maximum ZT value is enhanced to 1.34 at $T = 1000$ K near the same n. Therefore, in our later discussion of strain effect on LaP, we

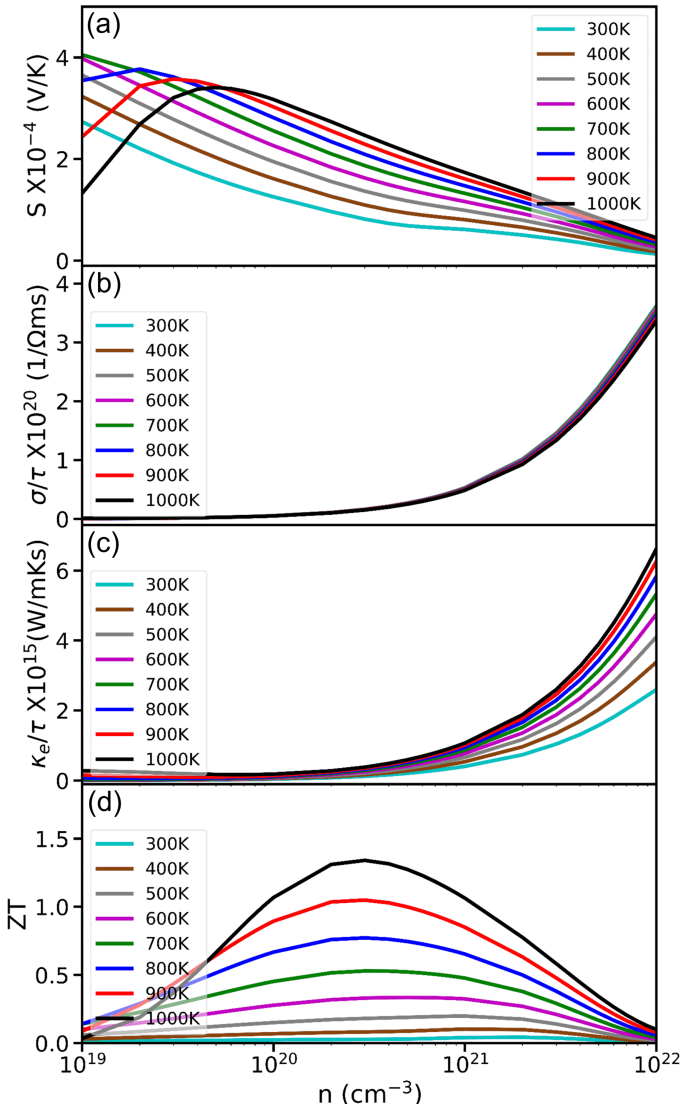

Fig. 4 Thermoelectric properties of unstrained LaP: (a) Seebeck coefficient S, (b) electrical conductivity σ divided by the relaxation time τ, (c) electronic thermal conductivity κ_e divided by τ, and (d) $ZT = S^2\sigma T/\kappa$, as a function of carrier concentration n in the temperature range $T = 300 - 1000$ K. The calculations are performed using the SCAN functional with scissor correction. The horizontal axis is in a log scale.

fix the carrier concentration to be $n = 3 \times 10^{20}$ cm^{-3} for potential optimal thermoelectric performance.

Figure 5 shows the lattice thermal conductivity κ_L of LaP as a function of T in the -2% (compressive) to +2% (tensile) isotropic strain range, which can potentially be achieved using only mechanical or piezoelectric devices, without more advanced diamond anvil cell techniques. Our calculations of corresponding phonon spectra and elastic constant matrices indicate that the cubic crystal structure remains dynamically and mechanically stable in this $\pm 2\%$ strain range. Notably, κ_L decreases with increasing T, and behaves as $\kappa_L \sim T^{-1}$ at high temperature[63]. This behavior can be understood qualitatively using kinetic theory and the Debye model:

$$\kappa_L = \frac{1}{3} v_s^2 c_v \tau_s. \quad (4)$$

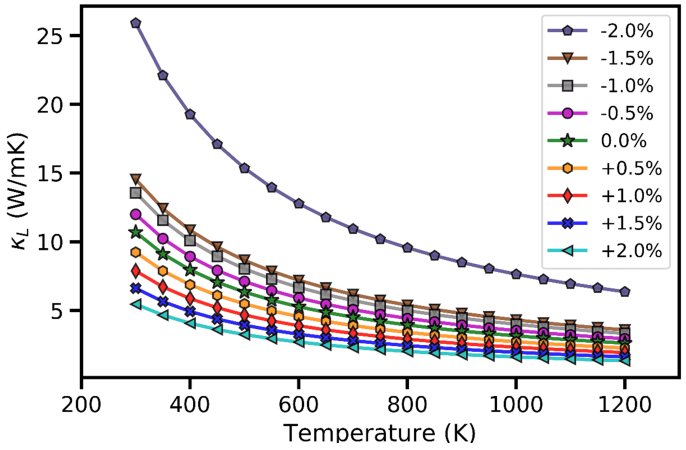

Fig. 5 Lattice thermal conductivity κ_L as a function of temperature for LaP in the isotropic strain range -2% to $+2\%$.

Here, v_s and c_v are respectively the phonon velocity and specific heat. In Debye model, v_s has no temperature dependence, and c_v is only weakly dependent on T above the Debye temperature Θ_D. τ_s is the phonon relaxation time (or equivalently, τ_s^{-1} is the phonon scattering rate). Therefore, the temperature dependence of κ_L at $T \gg \Theta_D$ is governed by τ_s, which is inversely proportional to the phonon occupation number $n_s(\mathbf{q}) \sim k_B T/\hbar\omega_s(\mathbf{q})$ at high temperature. Therefore, κ_L scales as $\sim T^{-1}$ at $T \gg \Theta_D$. Also as shown in Fig. 5, κ_L is reduced (enhanced) by a tensile (compressive) strain, due to a softening (hardening) of the phonon velocity. Finally, we note that PHONO3PY considers only three-phonon scattering processes. If four-phonon processes are also included, $\kappa_L \sim (T + \alpha T^2)^{-1}$ will be further reduced (and ZT will be further enhanced accordingly).

We next discuss the effect of isotropic strain on other transport coefficients and the ZT value, by fixing the carrier concentration at $n = 3 \times 10^{20}$ cm^{-3}. Figure 6(a) shows the temperature evolution of Seebeck coefficient S for strain values ranging from -2% to $+2\%$. As discussed before, S will increase with T, except when the bipolar effect sets in at higher temperature. In addition, S can be enhanced by a tensile strain, mainly due to an increased carrier effective mass m^* by strain engineering. This is consistent with the behavior of the electrical conductivity σ shown in Fig. 6(b), where σ is reduced by a tensile strain (as $\sigma \propto 1/m^*$). Similar to σ, the electronic thermal conductivity κ_e is reduced by a tensile strain, while κ_e uplifts with increasing T. These behaviors are consistent with the Wiedemann-Franz law in Eq. (3). Since a tensile strain can enhance S and meanwhile reduce both κ_e and κ_L, the ZT value is expected to increase accordingly. Indeed, Fig. 6(d) shows that the ZT value strongly depends on the temperature and applied strain. In general, ZT is enhanced with increasing T and positive (tensile) strain. At $T = 1200$ K, the ZT value of LaP under a $+2\%$ tensile strain can exceed 2, which is enhanced by 90% compared to the unstrained value.

We last turn our discussion to LaAs, which is also dynamically stable in the rock-salt structure like LaP[†]. The relaxed lattice parameter of unstrained LaAs in a primitive cell is found to be $a = 4.379$ Å, which corresponds to $a = 6.193$ Å in a conventional

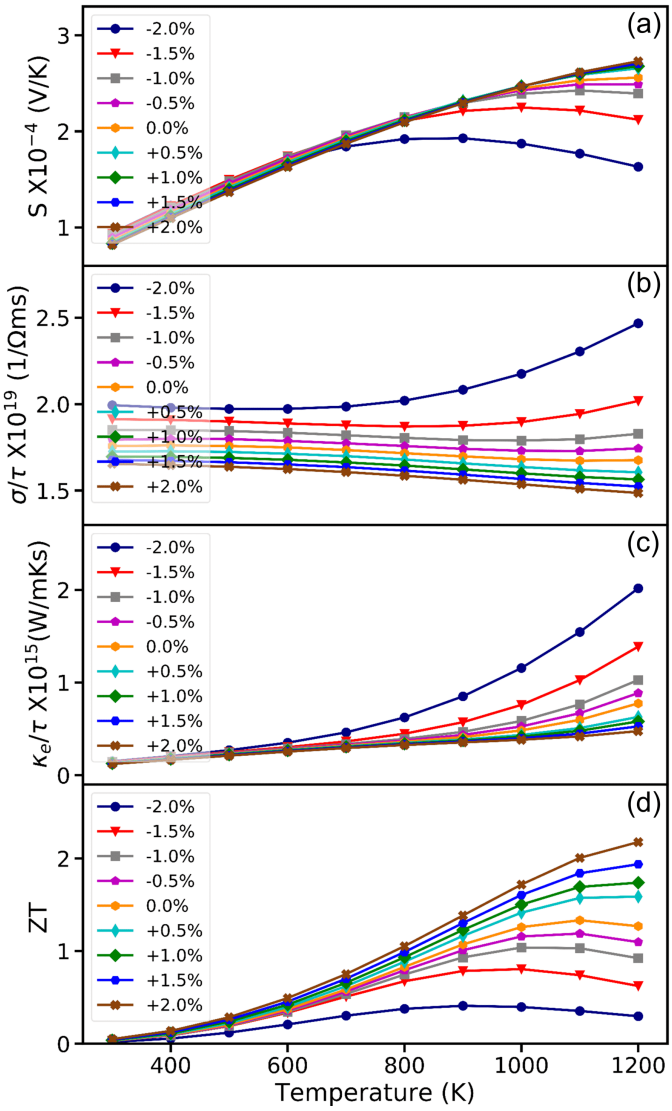

Fig. 6 Thermoelectric properties of LaP in the isotropic strain range -2% to $+2\%$: (a) Seebeck coefficient S, (b) electrical conductivity σ divided by the relaxation time τ, (c) electronic thermal conductivity κ_e divided by τ, and (d) $ZT = S^2\sigma T/\kappa$, as a function of temperature. The calculations are performed using the SCAN functional with scissor correction at carrier concentration $n = 3 \times 10^{20}$ cm^{-3}.

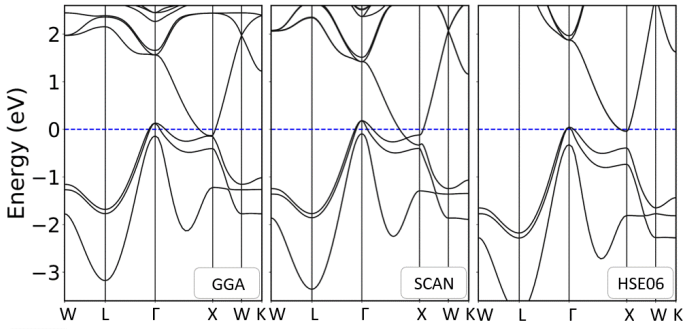

Fig. 7 Band structures along high-symmetry paths of the Brillouin zone computed respectively by GGA, SCAN, and HSE06 functionals for unstrained LaAs. The zero energy corresponds to the Fermi level.

cell. This value is also in agreement with previous reports of $a = 6.173$ Å[64] and $a = 6.182$ Å[41].

Figure 7 shows the band structures computed by different functionals for unstrained LaAs. Overall, LaAs has a band structure resembling that of LaP, albeit with a smaller energy gap at the X point[64]. In particular, LaAs remains a semimetal even with the HSE06 hybrid functional. This reduced gap size is consistent with electronegativity consideration: The band gap of a binary A-B compound is positively correlated with the atoms' electronegativity difference $|\chi_A - \chi_B|$[65]. In Paulin scale, $\chi_P > \chi_{As} > \chi_{Sb} > \chi_{Bi} > \chi_{La} = 1.1$. Therefore, the band gap of LaX would decease when X moves down along the pnictogen group in the periodic table, which agrees with DFT calculations[64].

Figure 8(a) shows the Seebeck coefficient S of LaAs as a function of carrier concentration n at various temperatures T. Compared to LaP, there are two salient features. First, the bipolar effect on LaAs is more severe, due to a narrower band gap which enhances thermal excitations of both charge and hole carriers. Second, LaAs has a smaller Seebeck coefficient. For example, the peak value of $S = 1.97$ at $T = 1000$ K in LaAs is reduced to roughly 60% of that in LaP. Because of a larger p-orbital spread, LaAs has a more dispersive band structure (with a smaller effective mass m^*), so a smaller S is anticipated.

Figures 8(b) and 8(c) show respectively the electrical conductivity σ and the electronic thermal conductivity κ_e, divided by the relaxation time τ. Their overall dependences on the carrier concentration and temperature follow similar trends to those discussed in Figs. 4(b) and 4(c) for LaP. The resulting ZT value of LaAs is shown in Fig. 8(d). At $T = 800$ K, ZT is peaked at $n = 7 \times 10^{20}$ cm^{-3}; the peak value of $ZT = 0.44$ is $\sim 60\%$ that of LaP at the same temperature. Therefore, LaAs has a lower thermoelectric performance. Nevertheless, the maximum ZT value of LaAs still could be boosted to near unity at $T \geq 1000$ K with applied strain, as seen in Fig. 9(d). We note that since the electrical conductivity σ is weakly temperature dependent [Fig. 9(b)], the temperature dependence of the power factor ($\equiv S^2\sigma$) is mainly determined by the Seebeck coefficient S [Fig. 9(a)].

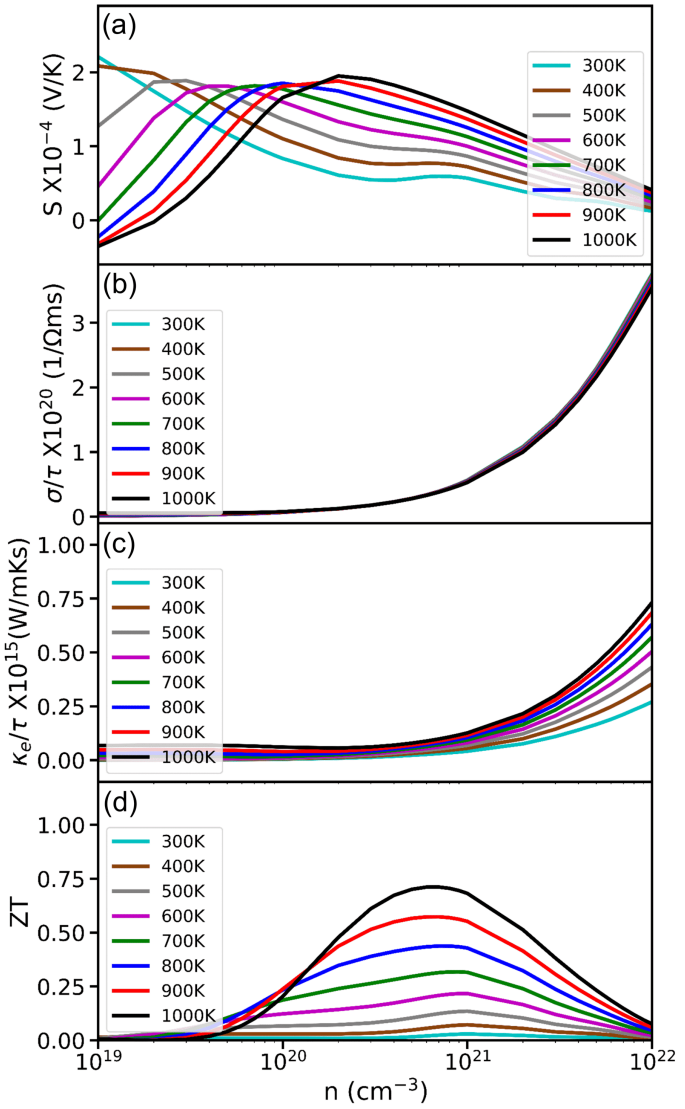

Fig. 8 Thermoelectric properties of unstrained LaAs: (a) Seebeck coefficient S, (b) electrical conductivity σ divided by the relaxation time τ, (c) electronic thermal conductivity κ_e divided by τ, and (d) $ZT = S^2\sigma T/\kappa$, as a function of carrier concentration n in temperature range $T = 300 - 1000$ K. The calculations are performed using the SCAN functional with scissor correction. The horizontal axis is in a log scale.

4 Conclusion

We have studied systematically rock-salt structured LaP and LaAs using first-principles calculations based on density functional the-

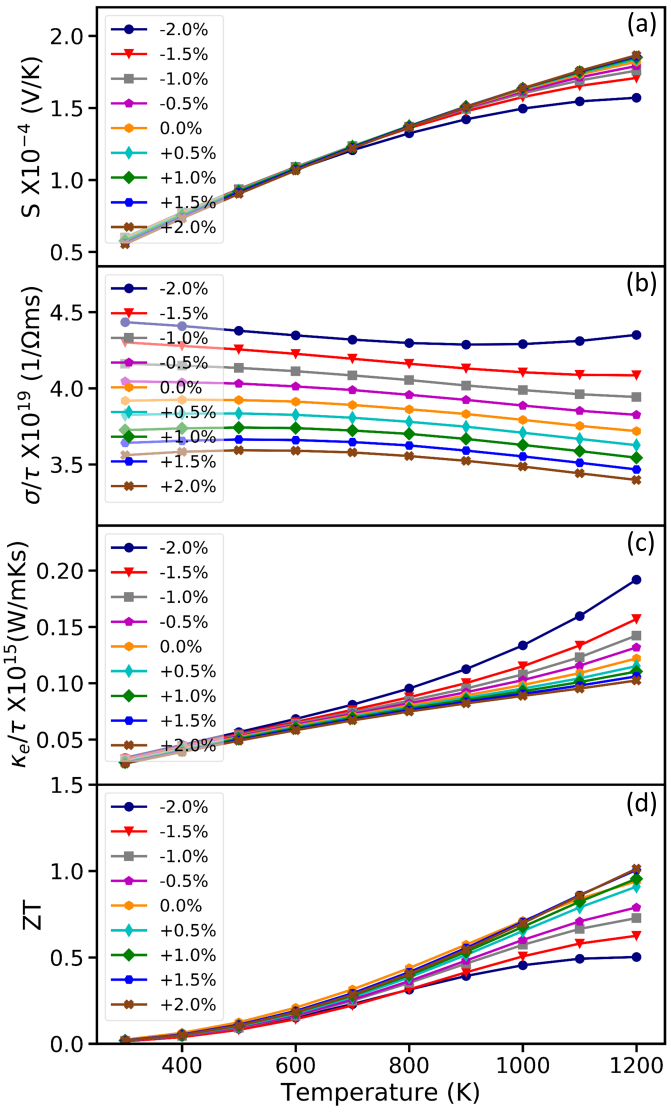

Fig. 9 Thermoelectric properties of LaAs in the isotropic strain range -2% to $+2\%$: (a) Seebeck coefficient S, (b) electrical conductivity σ divided by the relaxation time τ, (c) electronic thermal conductivity κ_e divided by τ, and (d) $ZT = S^2\sigma T/\kappa$, as a function of temperature. The calculations are performed using the SCAN functional with scissor correction at carrier concentration $n = 7 \times 10^{20}$ cm^{-3}.

ory. The employed metal-GGA functional with scissor correction method have enabled computationally efficient and precise evaluations of band structures and thermoelectric properties. We have shown that applying isotropic strain can effectively manipulate the thermoelectric performance. At the optimal carrier concentration $n = 3 \times 10^{20}$ cm^{-3}, $+2\%$ tensile strain can enhance the figure of merit ZT of LaP at $T = 1200$ K to > 2, which is 90% larger than the unstrained value. The transport coefficients of LaAs exhibit similar carrier concentration and temperature dependences to those of LaP. Due to a reduced band gap and a more dispersive band structure, the thermoelectric performance of LaAs is reduced with an optimal $ZT \sim 60\%$ that of LaP. With carrier doping and strain engineering, LaP and LaAs could be promising quantum materials for potential thermoelectric applications at high temperatures.

Finally, we note that LaSb and LaBi have even smaller band gaps and more dispersive bands (with smaller m^*). On general grounds, we thereby do not expect LaSb and LaBi to be of practical thermoelectric applications. However, these materials can exhibit nontrivial topological properties[66–70] for potential spintronic technologies.

Conflicts of interest

There are no conflicts to declare.

Acknowledgements

The calculations were performed on the Frontera computing system at the Texas Advanced Computing Center. Frontera is made possible by National Science Foundation award OAC-1818253.

Notes and references

1 J. Yang and T. Caillat, *MRS Bulletin*, 2006, **31**, 224–229.
2 M. W. Gaultois, T. D. Sparks, C. K. Borg, R. Seshadri, W. D. Bonificio and D. R. Clarke, *Chemistry of Materials*, 2013, **25**, 2911–2920.
3 X. Zhang and L.-D. Zhao, *Journal of Materiomics*, 2015, **1**, 92–105.
4 I. Petsagkourakis, K. Tybrandt, X. Crispin, I. Ohkubo, N. Satoh and T. Mori, *Science and Technology of Advanced Materials*, 2018, **19**, 836–862.
5 M. Wolf, R. Hinterding and A. Feldhoff, *Entropy*, 2019, **21**, 1058.
6 D. Beretta, N. Neophytou, J. M. Hodges, M. G. Kanatzidis, D. Narducci, M. Martin-Gonzalez, M. Beekman, B. Balke, G. Cerretti, W. Tremel *et al.*, *Materials Science and Engineering: R: Reports*, 2019, **138**, 100501.
7 A. M. Dehkordi, M. Zebarjadi, J. He and T. M. Tritt, *Materials Science and Engineering: R: Reports*, 2015, **97**, 1–22.
8 S. Twaha, J. Zhu, Y. Yan and B. Li, *Renewable and Sustainable Energy Reviews*, 2016, **65**, 698–726.
9 P. Gorai, V. Stevanović and E. S. Toberer, *Nature Reviews Materials*, 2017, **2**, 1–16.
10 J. P. Heremans, V. Jovovic, E. S. Toberer, A. Saramat, K. Kurosaki, A. Charoenphakdee, S. Yamanaka and G. J. Snyder, *Science*, 2008, **321**, 554–557.
11 Y. Pei, X. Shi, A. LaLonde, H. Wang, L. Chen and G. J. Snyder, *Nature*, 2011, **473**, 66–69.
12 N. Hinsche, I. Mertig and P. Zahn, *Journal of Physics: Condensed Matter*, 2012, **24**, 275501.
13 L. Xi, J. Yang, L. Wu, J. Yang and W. Zhang, *Journal of Materiomics*, 2016, **2**, 114–130.
14 E. B. Isaacs and C. Wolverton, *Physical Review Materials*, 2019, **3**, 015403.
15 K. Kaur, S. Dhiman and R. Kumar, *Materials Research Express*, 2017, **4**, 075509.
16 S. Wei, C. Wang, S. Fan and G. Gao, *Journal of Applied Physics*, 2020, **127**, 155103.
17 N. Xu, Y. Xu and J. Zhu, *npj Quantum Materials*, 2017, **2**, 51.

18 J. Gooth, G. Schierning, C. Felser and K. Nielsch, *MRS Bulletin*, 2018, **43**, 187–192.

19 C. Glassbrenner and G. A. Slack, *Physical Review*, 1964, **134**, A1058.

20 R. Berman and P. G. Klemens, *PhT*, 1978, **31**, 56.

21 H. Shi, D. Parker, M.-H. Du and D. J. Singh, *Physical Review Applied*, 2015, **3**, 014004.

22 J. Gong, A. Hong, J. Shuai, L. Li, Z. Yan, Z. Ren and J.-M. Liu, *Physical Chemistry Chemical Physics*, 2016, **18**, 16566–16574.

23 F. Hulliger, *Handbook on the Physics and Chemistry of Rare Earths*, 1979, **4**, 153–236.

24 S. Kimura, F. Arai, Y. Haga, T. Suzuki and M. Ikezawa, *Physica B: Condensed Matter*, 1995, **206**, 780–782.

25 A. Petukhov, W. Lambrecht and B. Segall, *Physical Review B*, 1996, **53**, 4324.

26 G. Vaitheeswaran, V. Kanchana and M. Rajagopalan, *Physica B: Condensed Matter*, 2002, **315**, 64–73.

27 I. Shirotani, K. Yamanashi, J. Hayashi, N. Ishimatsu, O. Shimomura and T. Kikegawa, *Solid State Communications*, 2003, **127**, 573–576.

28 G. Pagare, S. P. Sanyal and P. Jha, *Journal of Alloys and Compounds*, 2005, **398**, 16–20.

29 S. D. Gupta, S. K. Gupta and P. K. Jha, *Computational Materials Science*, 2010, **49**, 910–915.

30 N. Kumar, C. Shekhar, S.-C. Wu, I. Leermakers, O. Young, U. Zeitler, B. Yan and C. Felser, *Physical Review B*, 2016, **93**, 241106.

31 Y. Zhou, Y. Cheng, X.-R. Chen, C.-E. Hu and Q.-F. Chen, *Philosophical Magazine*, 2018, **98**, 1900–1918.

32 Y. Zhou, W.-L. Tao, Z.-Y. Zeng, X.-R. Chen and Q.-F. Chen, *Journal of Applied Physics*, 2019, **125**, 045107.

33 A. Hasegawa, *Journal of Physics C: Solid State Physics*, 1980, **13**, 6147.

34 M. Norman, H. Jansen, D. Koelling and A. J. Freeman, *Solid State Communications*, 1984, **52**, 739–741.

35 G. Gökoğlu and A. Erkişi, *Solid State Communications*, 2008, **147**, 221–225.

36 Y. Ciftci, K. Colakoglu, E. Deligoz and H. Ozisik, *Materials Chemistry and Physics*, 2008, **108**, 120–123.

37 E. Deligöz, K. Çolakoğlu, Y. Ö. Çiftçi and H. Özişik, *Journal of Physics: Condensed Matter*, 2007, **19**, 436204.

38 Z. Charifi, A. H. Reshak and H. Baaziz, *Solid State Communications*, 2008, **148**, 139–144.

39 M. Shoaib, G. Murtaza, R. Khenata, M. Farooq and R. Ali, *Computational Materials Science*, 2013, **79**, 239–246.

40 Z. Wu and R. E. Cohen, *Physical Review B*, 2006, **73**, 235116.

41 X. Yan, Y. Chen, X. Kuang and S. Xiang, *Journal of Applied Physics*, 2014, **116**, 083707.

42 S. Khalid, A. Sharan and A. Janotti, *Physical Review B*, 2020, **101**, 125105.

43 J. P. Perdew and K. Schmidt, AIP Conference Proceedings, 2001, pp. 1–20.

44 P. Hohenberg and W. Kohn, *Physical Review*, 1964, **136**, B864.

45 W. Kohn and L. J. Sham, *Physical Review*, 1965, **140**, A1133.

46 G. Kresse and J. Furthmüller, *Computational Materials Science*, 1996, **6**, 15–50.

47 G. Kresse and J. Furthmüller, *Physical Review B*, 1996, **54**, 11169.

48 J. P. Perdew, K. Burke and M. Ernzerhof, *Physical Review Letters*, 1996, **77**, 3865.

49 J. Sun, A. Ruzsinszky and J. P. Perdew, *Physical Review Letters*, 2015, **115**, 036402.

50 J. Heyd, G. E. Scuseria and M. Ernzerhof, *The Journal of Chemical Physics*, 2003, **118**, 8207–8215.

51 E. N. Brothers, A. F. Izmaylov, J. O. Normand, V. Barone and G. E. Scuseria, *The Journal of Chemical Physics*, 2008, **129**, 011102.

52 H. J. Monkhorst and J. D. Pack, *Physical Review B*, 1976, **13**, 5188.

53 G. K. Madsen, J. Carrete and M. J. Verstraete, *Computer Physics Communications*, 2018, **231**, 140–145.

54 G. Mahan and J. Sofo, *Proceedings of the National Academy of Sciences*, 1996, **93**, 7436–7439.

55 A. Togo and I. Tanaka, *Scripta Materialia*, 2015, **108**, 1–5.

56 A. Togo, L. Chaput and I. Tanaka, *Physical Review B*, 2015, **91**, 094306.

57 K. Mizokami, A. Togo and I. Tanaka, *Physical Review B*, 2018, **97**, 224306.

58 K. Momma and F. Izumi, *Journal of Applied Crystallography*, 2011, **44**, 1272–1276.

59 B. Patra, S. Jana, L. A. Constantin and P. Samal, *Physical Review B*, 2019, **100**, 045147.

60 M. Cutler, J. F. Leavy and R. L. Fitzpatrick, *Physical Review*, 1964, **133**, A1143–A1152.

61 G. J. Snyder and E. S. Toberer, *Nature Materials*, 2008, **7**, 105–114.

62 G. Chester and A. Thellung, *Proceedings of the Physical Society*, 1961, **77**, 1005.

63 E. S. Toberer, A. Zevalkink and G. J. Snyder, *Journal of Materials Chemistry*, 2011, **21**, 15843–15852.

64 S. Khalid, F. P. Sabino and A. Janotti, *Physical Review B*, 2018, **98**, 220102.

65 F. Di Quarto, C. Sunseri, S. Piazza and M. C. Romano, *The Journal of Physical Chemistry B*, 1997, **101**, 2519–2525.

66 M. Zeng, C. Fang, G. Chang, Y.-A. Chen, T. Hsieh, A. Bansil, H. Lin and L. Fu, *arXiv:1504.03492*, 2015.

67 Y. Wu, T. Kong, L.-L. Wang, D. D. Johnson, D. Mou, L. Huang, B. Schrunk, S. L. Bud'ko, P. C. Canfield and A. Kaminski, *Physical Review B*, 2016, **94**, 081108.

68 L.-K. Zeng, R. Lou, D.-S. Wu, Q. N. Xu, P.-J. Guo, L.-Y. Kong, Y.-G. Zhong, J.-Z. Ma, B.-B. Fu, P. Richard, P. Wang, G. T. Liu, L. Lu, Y.-B. Huang, C. Fang, S.-S. Sun, Q. Wang, L. Wang, Y.-G. Shi, H. M. Weng, H.-C. Lei, K. Liu, S.-C. Wang, T. Qian, J.-L. Luo and H. Ding, *Physical Review Letters*, 2016, **117**, 127204.

69 J. Nayak, S.-C. Wu, N. Kumar, C. Shekhar, S. Singh, J. Fink, E. E. D. Rienks, G. H. Fecher, S. S. P. Parkin, B. Yan and C. Felser, *Nature Communications*, 2017, **8**, 13942.

70 P.-J. Guo, H.-C. Yang, K. Liu and Z.-Y. Lu, *Physical Review B*, 2017, **96**, 081112.